Structure-Property Correlation for Niobium Nitride Superconductors for Ultra-Low Energy Applications

Osama Khalid Othman Batouk, **Dr Niladri Banerjee (Mentor)**

osama.batouk@kaust.edu.sa, n.banerjee@imperial.ac.uk

Abstract

Nine NbN thin films were grown on MgO by pulsed laser deposition at nitrogen pressures from 0 to 70 mTorr and scanned by atomic force microscopy. The aim was to find out which features of the film surface track the superconducting transition temperature T_c: the droplets that pulsed laser deposition leaves on the film, or the film surface between them. The answer is the film surface. Its roughness correlates with T_c at $r = -0.66$ and with resistivity at $r = +0.83$, and it is the only surface quantity whose correlation survives a change in how droplets are detected. Droplet size, number, density and coverage - the features that dominate the appearance of these images - show no relationship to T_c at all ($|r| \leq 0.39$). A simple gas-kinetic calculation predicts this contrast in advance. NbN loses about a third of its energy in each collision with N_2 and needs roughly twenty collisions to reach thermal energy, which happens near 31 mTorr for this geometry. Droplets are a hundred thousand times heavier and travel in straight lines at every pressure used. The gas therefore controls the flux that builds the film but not the flux that makes the droplets, and only the first of these correlates with T_c. Structural data on the same films support this reading: at a fixed number of laser pulses the films become thicker as the pressure rises, from 20 to 28 nm, which is what porous growth looks like. Consistent with all of it, T_c peaks at 12.45 K at 15 mTorr while resistivity and roughness reach their minima at 25 mTorr, and above 30 mTorr T_c falls by a factor of four.

Date: August 24, 2026

Correspondence: osama.batouk@kaust.edu.sa

Contents

1 Introduction **2**

1.1 Niobium nitride and why it matters . . . 2
1.2 Growth by pulsed laser deposition . . . 2
1.3 What Li *et al.* found . . . 2
1.4 Aim and scope . . . 3

2 Related Work **3**

3 Methodology **3**

3.1 Film growth and transport measurements . . . 4
3.2 AFM acquisition . . . 4
3.3 Corrections applied . . . 4
3.4 Droplet detection and roughness measurement . . . 4
3.5 What a scan looks like . . . 5
3.6 Detector validation . . . 5

4 The Kinetics of the Nitrogen Background Gas **6**

4.1 What leaves the target . . . 6
4.2 Mean free path and collision number . . . 6
4.3 Energy loss and the thermalisation threshold . . . 7
4.4 Sensitivity of the threshold . . . 8
4.5 Independent support from the growth study . . . 9
4.6 A prediction about droplets . . . 9

5 Results **9**

5.1 Transport . . . 9
5.2 Film roughness . . . 11
5.3 Droplet statistics . . . 12
5.4 Droplet size distributions . . . 15
5.5 Correlations with T_c . . . 18

6 Discussion **21**

6.1 Three growth regimes, set by the plume energy . . . 21
6.2 Roughness as a proxy for microstructure . . . 22
6.3 The null result on droplets, and why it was predictable . . . 23
6.4 The droplet height drift is most likely a threshold artefact . . . 23

7 Conclusion **24**

A Full Set of Droplet Size Distributions **25**

A.1 Radius distributions . . . 25
A.2 Height distributions . . . 29

References **32**

1 Introduction

1.1 Niobium nitride and why it matters

Niobium nitride is one of the most useful superconducting materials in practical electronics. In its cubic δ-NbN phase it superconducts up to about 17 K in bulk, it is hard and chemically stable, and it can be patterned into working devices [1, 2]. It is the standard material for superconducting nanowire single-photon detectors, and it is also used in high-inductance resonators, Josephson junction mixers and hot-electron bolometers for terahertz detection [2].

These applications need three things at once: a high transition temperature, a sharp transition, and a surface smooth enough for fine lithography. None of them is guaranteed by choosing NbN. The Nb-N system has several crystal phases - cubic δ, hexagonal β and tetragonal γ - with very different transition temperatures, and which one forms depends on the growth conditions rather than on the material [2, 3].

1.2 Growth by pulsed laser deposition

In pulsed laser deposition (PLD) a laser pulse removes material from a target, and the resulting plume travels through a background gas and condenses on a heated substrate [4]. The films studied here were grown by Li *et al.* [2] from a stoichiometric NbN target, not from metallic niobium, with nitrogen as the background gas.

That choice matters for how the results should be read. When a metallic target is used, the nitrogen has to supply every nitrogen atom in the film, so pressure is mainly a chemical variable. With an NbN target the plume already carries nitrogen, and Li *et al.* report that the gas then acts mainly as an inert ballast that slows the fastest particles down, changing the stoichiometry only slightly and not changing the phase. Their x-ray diffraction supports this: the NbN (002) peak does not shift significantly across the whole pressure range, and reciprocal space mapping finds cubic δ-NbN at every pressure, including 0 mTorr.

Nitrogen pressure in this series is therefore mostly a *kinetic* knob. It sets how many collisions an ablated atom suffers on its way to the substrate, and so how much energy it still carries when it lands. This is not a small effect. Species leaving a PLD target carry tens to hundreds of electron-volts [5, 6], while thermal evaporation delivers atoms at a few hundredths of an electron-volt. The background gas moves the process between these two extremes, and the whole range of film microstructures lies in between.

1.3 What Li *et al.* found

Li *et al.* measured T_c, lattice parameter and carrier concentration for this series [2]. They found a strongly non-monotonic T_c that peaks near 15 mTorr, and showed that it follows the out-of-plane lattice parameter almost linearly. Using the Allen-Dynes strong-coupling model they explained the variation as the combined effect of lattice strain and the electronic density of states at the Fermi level.

They also gave a physical account of how the strain arises. At very low pressure the arriving species are fast enough to peen the surface and implant below it, making a dense film under compressive stress. As pressure rises the gas slows the incoming ions. Above a certain pressure the fast particles are removed almost entirely and growth becomes porous and columnar. That is a description of the same kinetics this report calculates directly.

1.4 Aim and scope

This report asks a narrower question about the same films: which features of the surface, measured by AFM, track T_c, and can gas kinetics explain the answer?

The scope is limited to **surface morphology**: the size and number of the droplets that PLD leaves on the film, and the roughness of the NbN surface between them. Transition temperature and resistivity are taken from Li *et al.* [2] and used as the property side of the comparison; they were not measured here, and AFM cannot provide them.

The main result is a contrast. Film roughness tracks T_c and survives every robustness check applied to it. Droplet size, number, density and coverage do not, even though they dominate how these surfaces look. Section 4 shows that gas kinetics predicts exactly this contrast, because the two populations reach the substrate in completely different ways.

2 Related Work

Pressure selects the phase. Treece *et al.* showed that the phase produced by PLD on MgO (100) depends directly on the reactive gas pressure. Between 1 and 20 mTorr they obtained metallic Nb_2N, above 100 mTorr an insulating nitrogen-rich phase, and superconducting NbN only near 60 mTorr, where films reached $T_c = 16.6$ K and $J_c(4.2\ \text{K}) = 7.1$ MA cm^{-2} [1, 5]. Their work used a metallic Nb target, so pressure was acting chemically as well as kinetically.

Pressure controls the arrival energy. Farha *et al.* grew NbN_x over roughly 80-500 mTorr and found that raising the nitrogen background changed the phase from a mixture of cubic δ-NbN and hexagonal β-Nb_2N to single-phase β-Nb_2N, while the RMS roughness rose from 4.4 to 11.2 nm [7]. They attributed this to gas-phase kinetics: the background gas shortens the mean free path of the ablated species and lowers their kinetic energy, so lower pressure gives more mobile adatoms and a smoother film.

Structural order controls transport. Treece *et al.* grew films at the same time on MgO (100) and on amorphous fused silica. The oriented films reached 16.1 K with 60 $\mu\Omega$·cm, while the polycrystalline ones gave 11.8 K with 120 $\mu\Omega$·cm. They attributed the difference to grain-boundary scattering and a shorter electronic mean free path [1].

The films studied here. Li *et al.* grew and characterised this particular series [2]. Unlike the earlier PLD studies they used a stoichiometric NbN target, so nitrogen acts mainly as a ballast gas rather than as a reagent. They report a non-monotonic T_c peaking near 15 mTorr that follows the out-of-plane lattice parameter, and explain it with the Allen-Dynes model using the measured lattice parameter and density of states.

What is missing. None of this work separates the two things a PLD surface actually contains. AFM images of PLD films show both the film itself and the droplets thrown off the target, and published roughness values are usually taken over the whole scanned area, so the two are mixed together. This report measures them separately - droplet statistics on one side, film roughness between the droplets on the other - and asks which of them, if either, carries information about the superconducting properties.

3 Methodology

3.1 Film growth and transport measurements

The films were grown by Li *et al.* [2]. Their conditions are repeated here because several of them are needed for the calculation in Section 4. Deposition was by PLD in an ultra-high vacuum chamber with a base pressure of about 1.5×10^{-6} Pa, from a one-inch commercial target of 99.5% pure NbN, using a KrF excimer laser ($\lambda = 248$ nm) at 10 Hz with a fluence of 2.41 J·cm^{-2} for 9000 pulses, onto MgO (001) substrates held at 600 °C. Nitrogen partial pressure was the only variable that was deliberately changed.

Every film in the series, including the one grown with no nitrogen, came from the same NbN target. The 0 mTorr film is therefore an NbN film and a full member of the series, not a metallic niobium endpoint outside it. Li *et al.* confirm this directly: their diffraction data show cubic δ-NbN at 0 mTorr as at every other pressure. What makes that film unusual is not its phase but the fact that it received the most energetic flux of the series, with no gas to slow the plume down.

The transport series covers ten pressures (0, 5, 10, 15, 25, 30, 40, 50, 60 and 70 mTorr). The nine imaged here omit the 5 mTorr film, so every correlation in this report is over $n = 9$.

Critical temperature and resistivity were measured by four-point transport on the same samples [2], with T_c defined as the temperature where the resistance falls to half its normal-state value. Repeat measurements agree to about 10 mK, which is far smaller than the plotted symbols, so the T_c points carry no vertical error bars. The resistivity uncertainties are theirs.

3.2 AFM acquisition

Surfaces were imaged at 512×512 pixels with a pixel size of 37.4 nm, giving a field of view of about 19.16×19.16 μm. Three to five separate locations were imaged on each sample, 38 scans in total. Images were exported from Gwyddion as ASCII height matrices with the header comment kept, so the physical scan size could be read from the file rather than assumed.

3.3 Corrections applied

The field of view is not identical for every sample. Back-calculating the imaged area from droplet count and density gives scan sides of 18.33, 18.39, 19.16 and 20.00 μm depending on the sample. Raw droplet *count* is therefore not comparable between pressures, and droplet density (μm^{-2}) is used throughout instead.

One point of definition: roughness here is always measured on the NbN film surface *between* the droplets, never on bare substrate. It is reported as S_q (RMS roughness) and S_a (mean roughness).

3.4 Droplet detection and roughness measurement

Droplets were found and measured with a purpose-built detector. Each scan is line-corrected in two passes, with strong features masked so that a bright streak cannot drag a whole scan line. The background is then removed with a 51-pixel median filter, which follows the real waviness of the film without leaving the halo that a rolling-ball background produces around large features.

The important design choice is what a droplet is compared against. All detection thresholds are set as multiples of the film's own texture rather than of instrument noise, so the same settings behave consistently on a smooth scan and a rough one.

Seeds are found by h-maxima, so one droplet gives one seed rather than several. Each seed is grown by watershed until the surface falls back towards the local background; holes are filled, single-pixel nicks closed, and fragments merged where the saddle between them is too shallow to

be a real valley. Candidates then face eight acceptance tests - too small, is a pit, not a bump, line artefact, not compact, ragged, on a bad scan line, below minimum size - and every rejection is counted and reported.

Height is measured against the median of a ring around each droplet, so a droplet sitting on a slope is measured against its own surroundings. Radius is the equivalent-circle radius of the area at half that height (FWHM). Roughness is computed on the film only, with droplets dilated away and flagged scan lines excluded.

3.5 What a scan looks like

Figure 1 shows one scan at each stage of the processing, so that the quantities used later can be seen rather than only described.

The raw height image on the left is dominated by two things that are not the film: a slow shading from top to bottom, which is the sample tilt, and faint horizontal banding, which is scan-line offset from the microscope. Both are instrument effects, and both would contaminate a roughness value taken directly from this image. The droplets are already visible as bright spots, and a number of dark pits can be seen as well.

The centre panel is the same scan after line correction and background removal. The tilt and the banding are gone, the background sits flat, and the surface texture of the film itself becomes visible between the droplets. This is the image on which every measurement is made.

The right panel shows the 419 droplets the detector accepted, marked in red. Two features of the result are worth noting. The dark pits are not marked, since pits fail the bump test, and the large irregular feature at the left edge is accepted as a single droplet rather than as the several fragments a simple threshold would produce. Roughness is then computed only on the unshaded area, which is the film surface between the droplets, so the droplets contribute to the droplet statistics and nothing else.

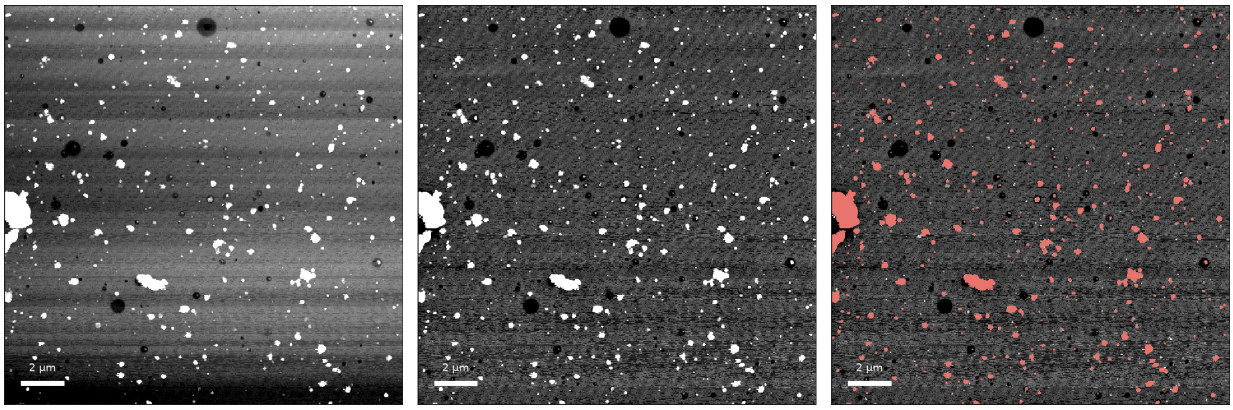


Figure 1 One scan at 10 mTorr (NbN_10mTorr_corner3). Left: raw height, with the tilt and scan-line offsets the microscope leaves. Centre: after line correction and background removal. Right: the 419 accepted droplets in red; roughness is measured only on the unshaded film between them.

3.6 Detector validation

Scored against every droplet rising more than 8 nm above the film surface, the detector misses 4-7% of them and captures 92-94% of the pixels belonging to those it finds. On synthetic ground truth it recovers radius to 1.003 and height to 0.971 of the true value, with no false positives and

no pit ever counted as a droplet. The few percent missed are small droplets touching a larger neighbour, which merge at the seeding stage.

4 The Kinetics of the Nitrogen Background Gas

This section works out what the background gas does to the two populations that land on the film. Every number in it is an order of magnitude estimate; the assumptions are stated as they are used, and their sensitivity is checked at the end.

4.1 What leaves the target

A PLD pulse is a violent event. The laser deposits energy into a sub-micron depth of the target in tens of nanoseconds, faster than heat can diffuse away, and the surface layer leaves as a dense plasma plume. What leaves is not describable by a single temperature: neutral atoms, ions, small clusters and, from the molten surface layer, macroscopic droplets, spanning many orders of magnitude in mass [6, 7].

The target used for these films is stoichiometric NbN rather than metallic niobium, so the plume already carries nitrogen with it and the droplets are fragments of molten NbN. The calculation below therefore takes the heavy plume species to be an NbN unit of mass 106.9 u. Section 4.4 shows that the result is not sensitive to this choice: taking atomic Nb instead moves the answer by about 10%, which is smaller than the other uncertainties in the estimate.

Two statements in the literature bracket the energy scale. Treece *et al.* report ions and neutrals with kinetic energies up to about 100 eV in their NbN growths [5], and Farha *et al.* quote several hundred eV from plume spectroscopy [7]. The estimates below take $E_0 = 100$ eV, at the conservative end. Nothing that follows depends strongly on this choice, because the energy falls geometrically with collision number.

4.2 Mean free path and collision number

An ablated species travelling through stationary N_2 has a mean free path

$$\lambda = \frac{1}{n\sigma}, \qquad n = \frac{P}{k_B T}, \tag{1}$$

where n is the gas number density and σ the collision cross-section. Taking $T = 300$ K for the bulk gas (the substrate is hot, the chamber gas is not) and $\sigma \approx 3.9 \times 10^{-19}$ m^2, which corresponds to a hard-sphere diameter of about 3.5 Å, gives the values in Table 1. Over the range studied λ falls from 8.0 mm at 10 mTorr to 1.1 mm at 70 mTorr.

What matters is not λ itself but its ratio to the target to substrate distance d, because that ratio is the number of collisions in transit:

$$N_{\mathrm{coll}} \simeq \frac{d}{\lambda} = n\sigma d. \tag{2}$$

The target to substrate distance was not recorded for this series, so $d = 50$ mm is assumed. That is a reasonable choice rather than an arbitrary one: Farha *et al.* used about 5 cm and Treece *et al.* about 6 cm [1, 7]. On that basis the collision number rises from about 6 at 10 mTorr to about 44 at 70 mTorr (Figure 2). The change from nearly ballistic transport to strongly collisional transport therefore happens inside this pressure series.

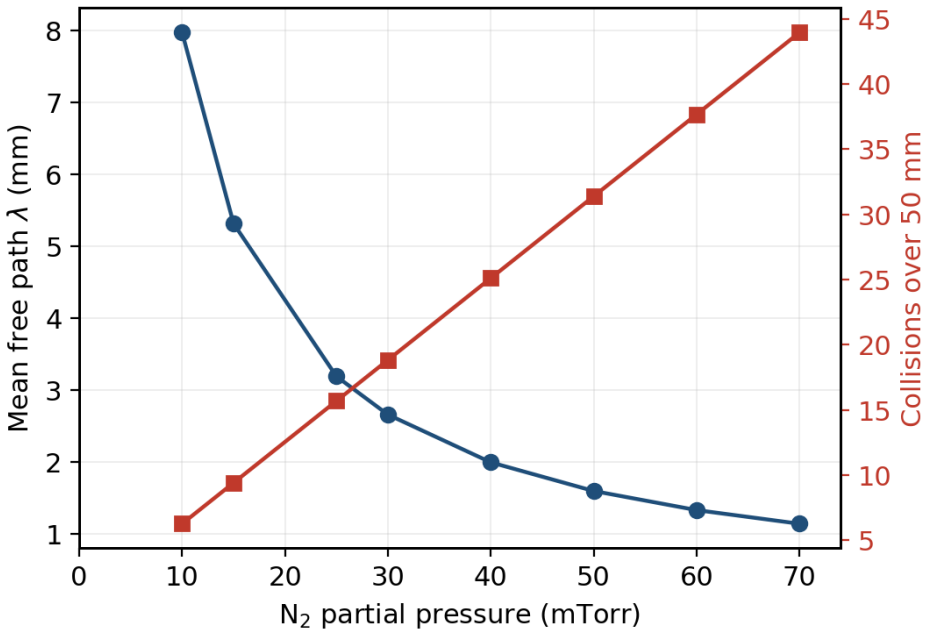


Figure 2 Mean free path of an ablated species in the N_2 background (dark blue, left axis) and the corresponding number of collisions over a 50 mm target to substrate distance (red, right axis).

4.3 Energy loss and the thermalisation threshold

For an elastic collision between masses m_1 and m_2, averaged over isotropic scattering, the mean fraction of energy transferred is

$$f = \frac{2m_1 m_2}{(m_1 + m_2)^2}. \tag{3}$$

For NbN (106.9 u) striking N_2 (28.0 u) this gives $f = 0.329$: an ablated unit loses just under a third of its energy in every collision. The exchange is efficient because the two masses are within a factor of four of each other. After N_{coll} collisions the surviving energy is

$$E \simeq E_0(1 - f)^{N_{\mathrm{coll}}}, \tag{4}$$

with a floor at the thermal energy of the gas, $\frac{3}{2}k_B T = 0.039$ eV at 300 K. Setting $E = \frac{3}{2}k_B T$ gives $N_{\mathrm{th}} = 19.7$: about twenty collisions bring a 100 eV species into equilibrium with the gas. Requiring these to happen within the target to substrate distance gives a characteristic pressure

$$P_{\mathrm{th}} = \frac{N_{\mathrm{th}} k_B T}{\sigma d} \approx 31 \text{ mTorr}. \tag{5}$$

Below roughly 31 mTorr the flux arrives well above thermal energy, 8.2 eV at 10 mTorr and 2.3 eV at 15 mTorr, and keeps enough mobility to find low energy sites on the growing surface. Above it, the arriving flux is thermalised and adatoms depend on substrate temperature alone. The change is abrupt on a logarithmic scale: the arrival energy falls by more than two orders of magnitude between 10 and 30 mTorr (Figure 3).

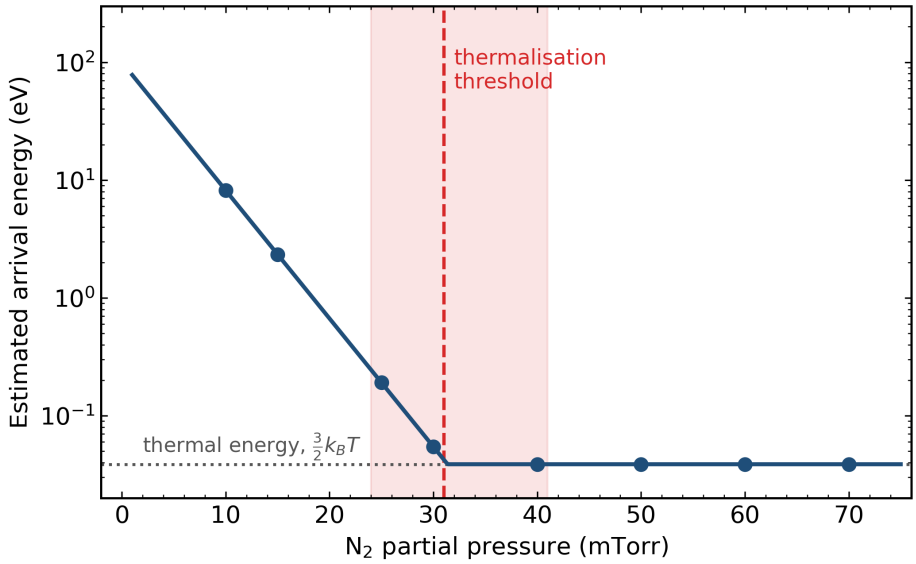


Figure 3 Estimated arrival energy against N_2 pressure, on a logarithmic scale. The dashed line marks the calculated thermalisation threshold and the shaded band its uncertainty; the dotted line is the thermal energy floor $\frac{3}{2}k_BT$ at 300 K.

Table 1 Gas-kinetic parameters at each nitrogen pressure. Mean free path and collision number assume $\sigma = 3.9 \times 10^{-19}$ m^2 and a 50 mm target to substrate distance; arrival energy assumes an NbN plume species with $E_0 = 100$ eV and is floored at the thermal energy of the gas.

P (mTorr)	λ (mm)	Collisions	Arrival energy (eV)
0	-	0	100 (assumed E_0)
10	7.97	6.3	8.17
15	5.31	9.4	2.34
25	3.19	15.7	0.19
30	2.66	18.8	0.055
40	1.99	25.1	thermal
50	1.59	31.4	thermal
60	1.33	37.7	thermal
70	1.14	43.9	thermal

4.4 Sensitivity of the threshold

The estimate is not precise, and it is worth being explicit about what moves it.

The plume species matters least. If the heavy species is atomic Nb (92.9 u) rather than NbN, the transferred fraction rises from 0.329 to 0.356 and the threshold falls from 31 to 28 mTorr, a shift of about 10%. Any heavy species between roughly 90 and 110 u gives a threshold in the same window. Only a much heavier fragment would move it appreciably, and clusters that large are a minor part of a PLD plume.

The geometry and the cross-section matter more. Varying the cross-section over 3.0 to 5.0×10^{-19} m^2 moves P_{th} between 41 and 24 mTorr; varying d over 40 to 60 mm moves it between 39 and 26 mTorr.

A fair statement is $P_{\mathrm{th}} = 31^{+10}_{-7}$ mTorr, or simply the middle of this pressure series. What should be taken from it is not the exact number but the fact that the transition falls inside the range studied, which is a claim the data can test.

4.5 Independent support from the growth study

This picture is close to the account Li *et al.* give from structural data alone [2]. They describe three regimes in the same order. At the lowest pressures the ablated species arrive fast enough to peen the surface and implant below it, making a dense layer under large compressive stress. As pressure rises the incoming ions are partly slowed by the gas. Beyond a threshold the fastest particles are removed almost entirely and growth becomes porous and columnar.

Those are the ballistic, intermediate and thermalised regimes of this section, identified from lattice strain rather than from gas kinetics. The estimate above puts the crossover at 31^{+10}_{-7} mTorr; their lattice parameter peaks at 15 mTorr and has fallen below the bulk value by 50 mTorr, so their crossover lies in the same window. Two independent routes to the same boundary is stronger evidence than either alone.

4.6 A prediction about droplets

The same reasoning makes a sharp, falsifiable prediction about the droplets, and it is worth stating before looking at the data.

Droplets are not condensed from the vapour. They are macroscopic fragments of molten target material, thrown out by boiling and splashing at the target surface, and they leave the target already formed. Their transport is governed by inertia, not by molecular collisions.

Quantitatively: a droplet of radius 60 nm, the typical FWHM radius measured here, with the density of NbN (about 8400 kg m^{-3}) has a mass of about 8×10^{-18} kg, some 5×10^{9} atomic mass units. Its stopping distance in a gas of density ρ_g is of order $(4/3)(\rho_d/\rho_g)r$. At 70 mTorr the N_2 density is 1.0×10^{-4} kg m^{-3}, giving a stopping distance of about **6.5 m**, more than two orders of magnitude further than the 50 mm the droplet has to travel.

Droplets are therefore ballistic at every pressure in this series. The gas does not slow them, deflect them or change where they land. Whatever governs their size and number happens at the target surface, not in the gas phase.

The prediction follows immediately. **Film roughness, which is built by adatoms whose energy the gas controls, should track the deposition kinetics and therefore the film's electronic quality. Droplet size and number, which the gas does not touch, should not.**

5 Results

5.1 Transport

Figures 4 and 5 show T_c and resistivity across the series, with values in Table 2. The behaviour is not monotonic and divides into two parts.

From 0 to 15 mTorr, T_c rises steeply - from 7.35 K for the film grown with no nitrogen to 12.30 K at 10 mTorr and a maximum of 12.45 K at 15 mTorr - while resistivity falls from 148.5 to 131.4 $\mu\Omega$·cm. The films are already cubic δ-NbN at 0 mTorr [2], so this branch is not the nitride forming. It is the growth improving as the first few mTorr of gas take the edge off an otherwise unscattered, strongly implanting plume.

From 25 mTorr onwards the trend reverses and does not recover. T_c falls through 11.85 K at 25 mTorr, 9.55 K at 30, 8.55 K at 40, 6.55 K at 50, 4.75 K at 60 and 3.00 K at 70 mTorr, a factor of four below the peak. Resistivity does the opposite, passing through a minimum of 117.5 $\mu\Omega$·cm at 25 mTorr and rising to 496.1 $\mu\Omega$·cm at 70 mTorr, a factor of 4.2. Over this branch T_c correlates with pressure at $r = -0.99$ and resistivity at $r = +0.96$.

Across the full series T_c and resistivity are anticorrelated at $r = -0.88$ (Figure 16). This is the strongest correlation in the dataset and the expected one: a film with more scattering centres has both a higher normal-state resistivity and a lower transition temperature.

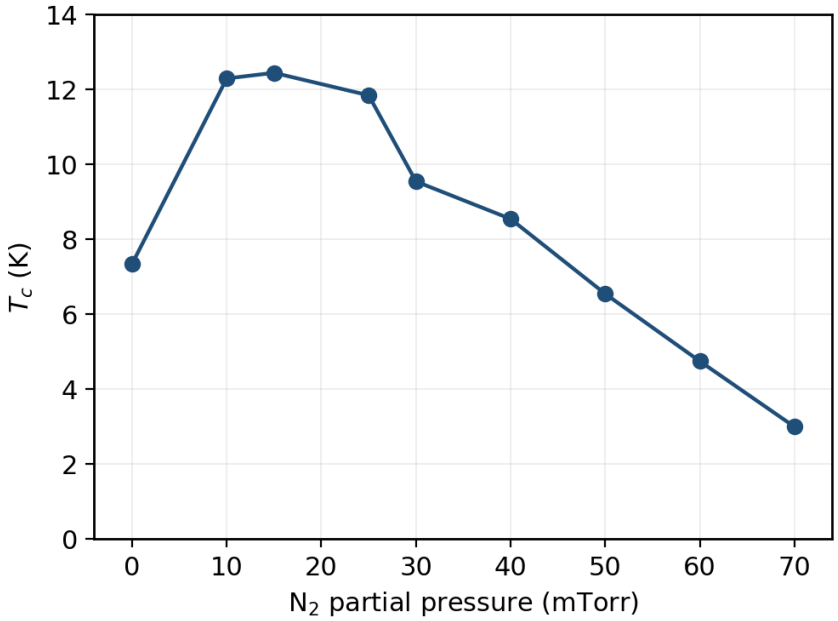


Figure 4 Superconducting transition temperature against N_2 partial pressure. Transport data from Li *et al.* [2]; no uncertainty is published for T_c.

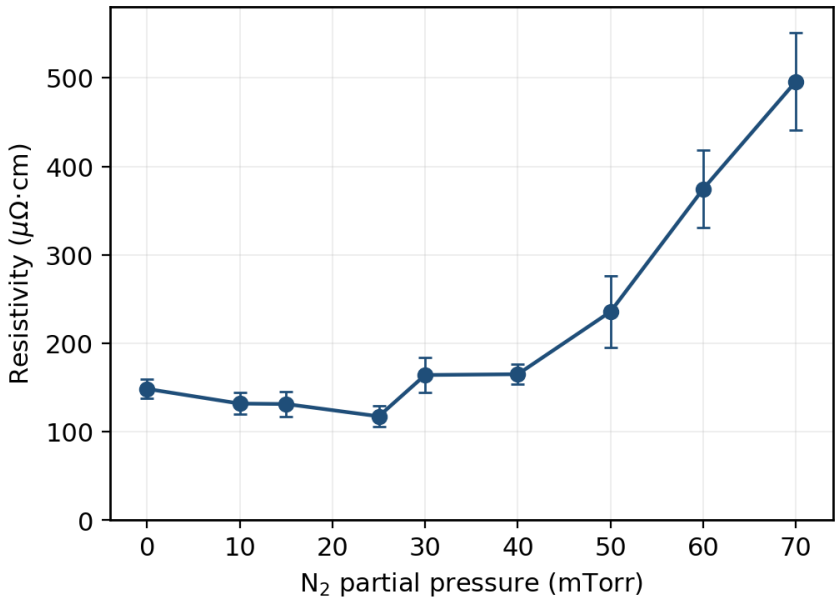


Figure 5 Normal-state resistivity against N_2 partial pressure. Error bars are the transport uncertainty quoted in [2].

Table 2 Transport properties and film roughness across the series. T_c and resistivity are from Li *et al.* [2]; roughness is measured in this work on the film surface between the droplets.

P (mTorr)	T_c (K)	ρ ($\mu\Omega$·cm)	S_q (nm)	S_a (nm)
0	7.35	148.5 ± 10.8	0.853 ± 0.250	0.619 ± 0.172
10	12.30	131.9 ± 12.2	1.408 ± 0.275	1.035 ± 0.147
15	12.45	131.4 ± 13.9	0.830 ± 0.107	0.618 ± 0.087
25	11.85	117.5 ± 11.6	0.735 ± 0.092	0.536 ± 0.058
30	9.55	164.2 ± 20.0	0.977 ± 0.391	0.692 ± 0.307
40	8.55	165.1 ± 11.0	0.770 ± 0.119	0.538 ± 0.072
50	6.55	235.8 ± 40.7	1.228 ± 0.254	0.887 ± 0.144
60	4.75	374.6 ± 43.9	1.944 ± 0.327	1.395 ± 0.267
70	3.00	496.1 ± 55.0	1.758 ± 0.326	1.291 ± 0.242

5.2 Film roughness

Roughness of the film surface between the droplets is plotted in Figure 6. Two things stand out.

First, the roughness minimum coincides with the transport optimum. S_q reaches its lowest value of 0.735 nm at 25 mTorr, in the same window where resistivity is lowest and T_c is near its maximum. From there it climbs to 1.228 nm at 50, 1.944 nm at 60 and 1.759 nm at 70 mTorr, a factor of 2.6 above the minimum. On the branch above 25 mTorr, S_q correlates with pressure at $r = +0.89$.

Second, the character of the roughness does not change even though its amplitude nearly triples. The ratio S_q/S_a is 1.382 ± 0.027 at every pressure, against 1.25 for a Gaussian height distribution. A constant ratio means the height distribution keeps the same shape while its width grows: the surface gets rougher in amplitude, not different in kind. Consistently with this, S_q and S_a correlate

with each other at $r = 0.999$, so only S_q need be quoted.

Roughness correlates with T_c at $r = -0.66$ (Figure 15) and with resistivity at $r = +0.83$ (Figure 19). The second of these is taken up in the discussion.

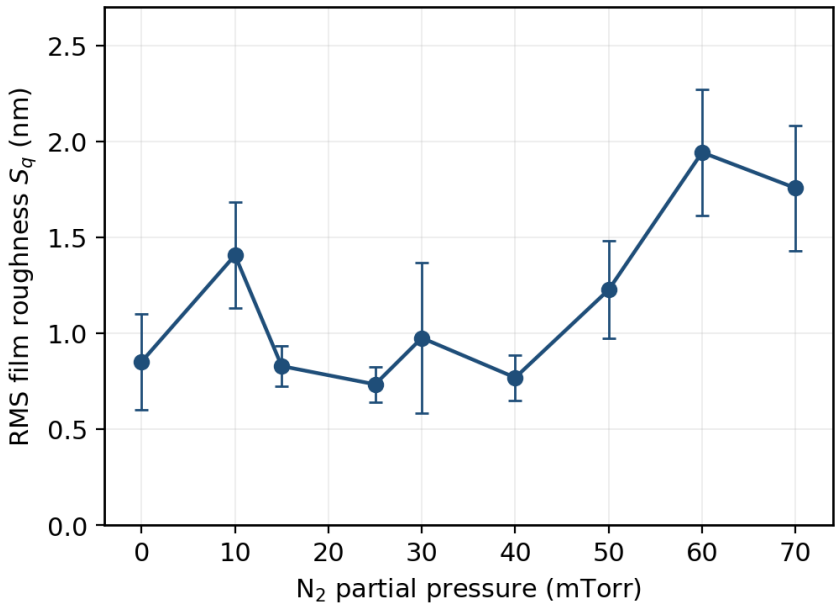


Figure 6 RMS roughness of the NbN film surface between the droplets, against N_2 partial pressure. Error bars are sample standard deviations across the 3-5 scans of each sample.

5.3 Droplet statistics

Droplet density, mean height, mean radius and area coverage are shown in Figures 7-10 and listed in Table 3. The droplets are abundant - 585 to 928 per scan, or 1.2 to 2.5 per μm^2 - and they dominate the appearance of every image, but their statistics behave quite differently from the roughness.

Density peaks at 2.53 μm^{-2} at 30 mTorr and shows no consistent trend with pressure ($r = +0.14$). Coverage varies between 4.2% and 9.2% with excursions at 25, 30 and 70 mTorr that form no pattern ($r = +0.39$). Mean radius stays between 58 and 82 nm with no clear ordering ($r = +0.37$). Only mean height shows a visible drift, rising from 19.4 nm at 0 mTorr to 37.7 nm at 70 mTorr ($r = +0.67$); Section 6.4 argues that this is a property of the detector rather than of the droplets.

The size distributions are strongly right-skewed at every pressure: a sharp peak just above the resolution limit with a long tail to large agglomerates. The medians therefore sit below the means (Table 4). At 0 mTorr, for instance, the median radius is 52 nm against a mean of 59.0 nm. The two numbers are not in conflict; they are different summaries of a skewed distribution, and the median is the more representative one.

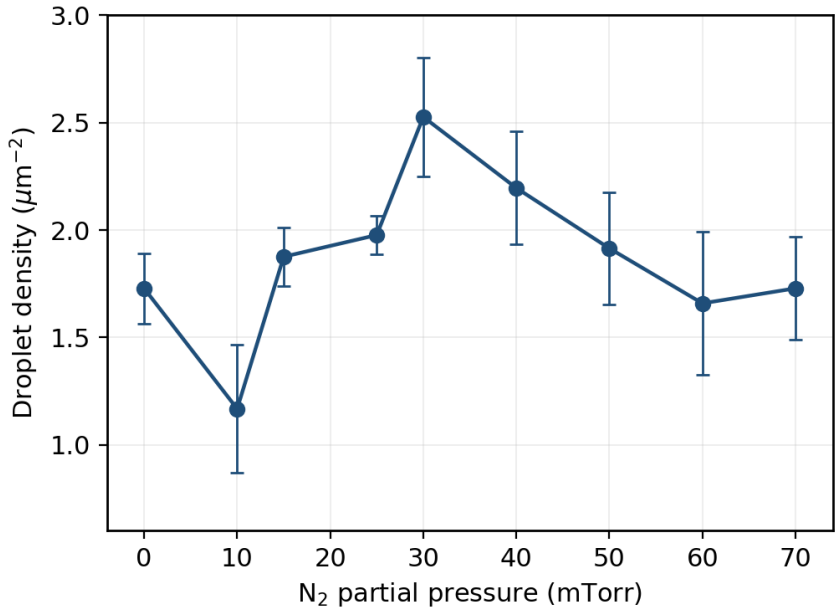


Figure 7 Droplet number density against N_2 partial pressure. Density rather than raw count is used because the imaged area is not identical for every sample.

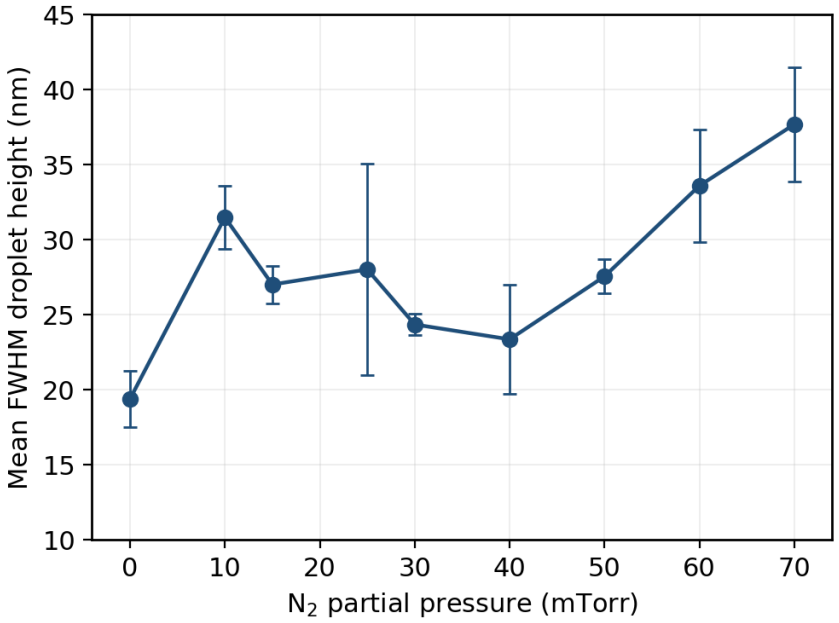


Figure 8 Mean FWHM droplet height against N_2 partial pressure - the only droplet quantity showing a discernible drift.

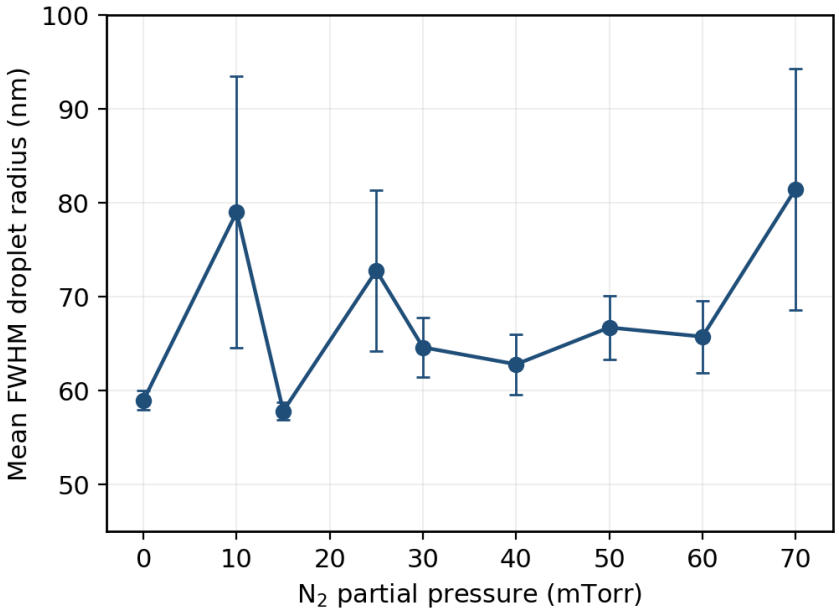


Figure 9 Mean FWHM droplet radius against N_2 partial pressure.

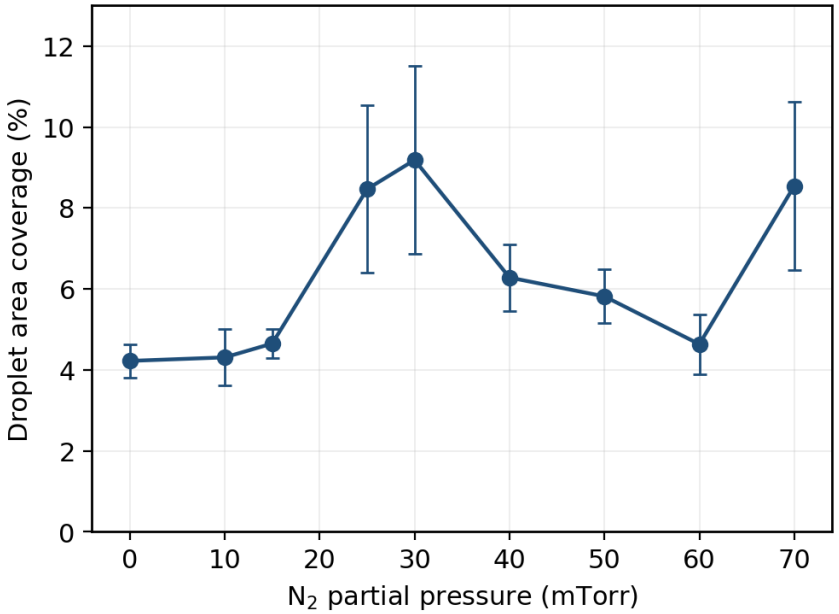


Figure 10 Fraction of the scanned area covered by droplets, against N_2 partial pressure.

Table 3 Droplet statistics, all-droplets analysis. Values are means over the scans of each sample; ± is the sample standard deviation across those scans.

P (mTorr)	Droplets/scan	Coverage (%)	Density (μm^{-2})	Height (nm)	Radius (nm)
0	635 ± 60	4.22 ± 0.41	1.729 ± 0.163	19.40 ± 1.88	58.99 ± 1.04
10	395 ± 101	4.31 ± 0.70	1.168 ± 0.299	31.50 ± 2.08	79.04 ± 14.46
15	689 ± 50	4.65 ± 0.35	1.876 ± 0.135	27.03 ± 1.26	57.85 ± 0.95
25	726 ± 33	8.47 ± 2.07	1.977 ± 0.090	28.03 ± 7.04	72.81 ± 8.58
30	928 ± 101	9.19 ± 2.32	2.527 ± 0.276	24.36 ± 0.71	64.64 ± 3.19
40	806 ± 96	6.28 ± 0.82	2.196 ± 0.263	23.37 ± 3.62	62.83 ± 3.21
50	691 ± 82	5.82 ± 1.14	1.915 ± 0.227	27.57 ± 2.61	66.75 ± 3.36
60	664 ± 91	4.64 ± 0.83	1.659 ± 0.228	33.61 ± 3.32	65.77 ± 3.05
70	585 ± 74	8.54 ± 2.29	1.729 ± 0.218	37.70 ± 4.14	81.51 ± 7.36

Table 4 Median droplet dimensions, pooled over all scans of each sample. Medians sit below the means of Table 3 because the distributions are strongly right-skewed.

P (mTorr)	Median FWHM radius (nm)	Median FWHM height (nm)
0	52	14.8
10	67	25.5
15	52	19.8
25	63	21.3
30	56	18.3
40	56	16.7
50	60	21.1
60	58	28.8
70	70	30.8

5.4 Droplet size distributions

The summary statistics above average over distributions whose shape carries information of its own. Figures 11-14 show the radius and height distributions at the two ends of the series; the full set is in Appendix A. Every panel uses identical axes and is normalised to the percentage of that sample's droplets in each bin, so the panels can be compared directly. Normalisation is necessary because three to five scans were pooled per pressure and the raw totals range from 1185 to 4640 droplets. The dotted line marks the median.

Three features matter.

The radius distribution keeps a fixed mode. At 0 mTorr the histogram peaks at about 45-50 nm; at 70 mTorr it peaks at about 45 nm. The peak does not move across the series. What changes is the weight of the right-hand tail: the modal bin falls from 24.7% to 16.9% of the population while the tail beyond 100 nm fills in, carrying the median from 52 to 70 nm. The distribution is not being rescaled by pressure; a tail of large agglomerates is being added to a population whose characteristic size is fixed.

This is a stronger test than the mean, and it is the test the ballistic argument of Section 4.6 specifically predicts. Stopping distance scales with droplet radius, so if the gas had any grip on

the droplets it would deplete the small-radius end first and the distribution would erode from the left. Evaluating the stopping length at 70 mTorr for the smallest resolvable droplets gives 1.1 m at $r = 10$ nm and 2.2 m at $r = 20$ nm, against a 50 mm flight. No size sorting is predicted anywhere in the range studied, and none is seen.

The shape is that of a fragmentation process. Every distribution is strongly right-skewed: a sharp peak a little above the resolution limit with a long tail. That is the generic signature of fragmentation - here, the splashing of a molten target surface - and not of condensation from a vapour, which gives narrower and more symmetric distributions. The histogram shape is thus independent evidence that these features arrive already formed rather than nucleating and growing on the film.

The film and the droplets behave differently. The ratio S_q/S_a is constant across the series, so the height distribution of the *film* surface also keeps a fixed shape while its width grows by a factor of 2.6. Placing that beside the droplet histograms gives the central result of this report in distributional terms: both populations are shape-invariant across the series, but only the film distribution changes scale with pressure. The gas rescales the height distribution of the film and leaves the size distribution of the droplets alone.

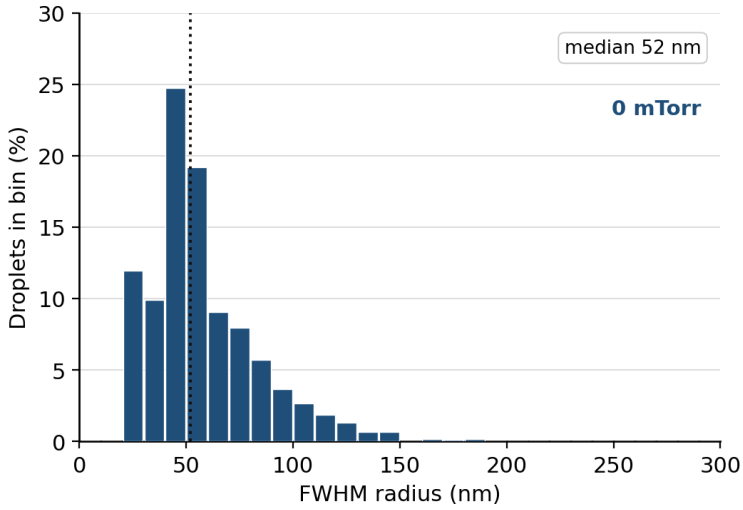


Figure 11 Droplet radius distribution at 0 mTorr, pooled over all scans and normalised to the percentage of droplets per bin. Dotted line: median.

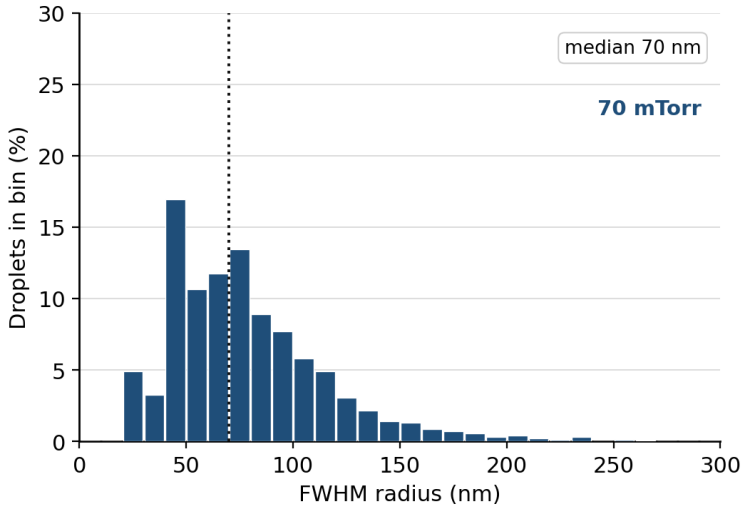


Figure 12 Droplet radius distribution at 70 mTorr. The mode remains at approximately 45 nm, as at 0 mTorr; the right-hand tail is heavier. Same axes as Figure 11.

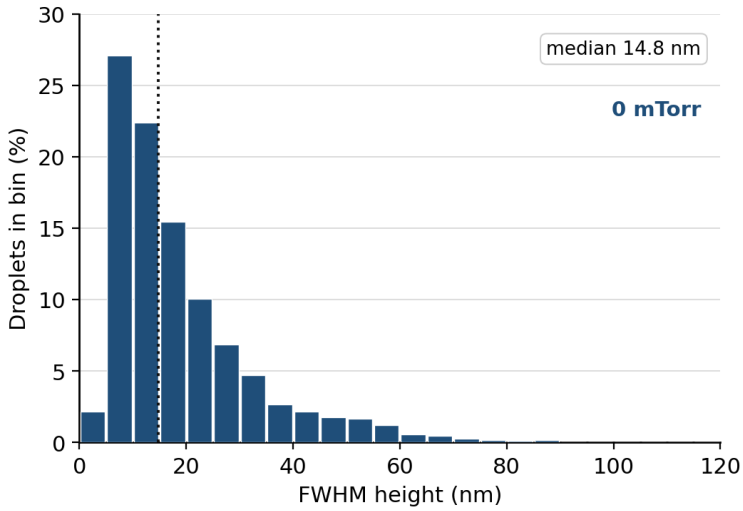


Figure 13 Droplet height distribution at 0 mTorr, with a large population of shallow droplets below 10 nm. Same axes as Figure 14.

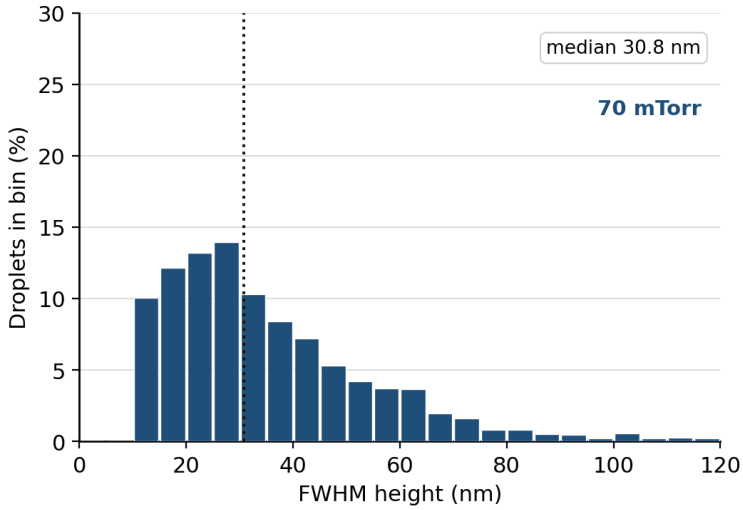


Figure 14 Droplet height distribution at 70 mTorr. Unlike the radius distribution, the whole distribution has translated upwards and the shallow population below 10 nm is absent. Section 6.4 argues this is most likely an artefact of the adaptive detection threshold rather than a change in the droplets.

5.5 Correlations with T_c

Table 5 and Figure 20 collect the Pearson correlation of each measured quantity with T_c across the nine samples. The ordering is unambiguous.

Table 5 Pearson correlation of each measured quantity with T_c, all-droplets analysis, nine samples.

Quantity	r with T_c
Resistivity	−0.88
RMS roughness S_q	−0.66
Mean roughness S_a	−0.65
Droplet FWHM height	−0.39
Droplet FWHM radius	−0.17
Droplet coverage	−0.12
Droplet count	−0.00
Droplet density	+0.01

There is a clear gap between the two roughness terms and everything to do with droplets. The critical test, though, is not the size of these numbers but their stability. Repeating the whole analysis with the stricter detection threshold - which changes droplet counts by roughly a factor of two - moves the roughness correlation from −0.66 to −0.71, slightly *stronger*, while the droplet terms move erratically and in some cases change sign: height from −0.39 to −0.23, radius from −0.17 to −0.10, density from +0.01 to −0.25.

A relationship that strengthens when the measurement is made more conservative is behaving like a relationship. One that weakens or flips sign is behaving like scatter.

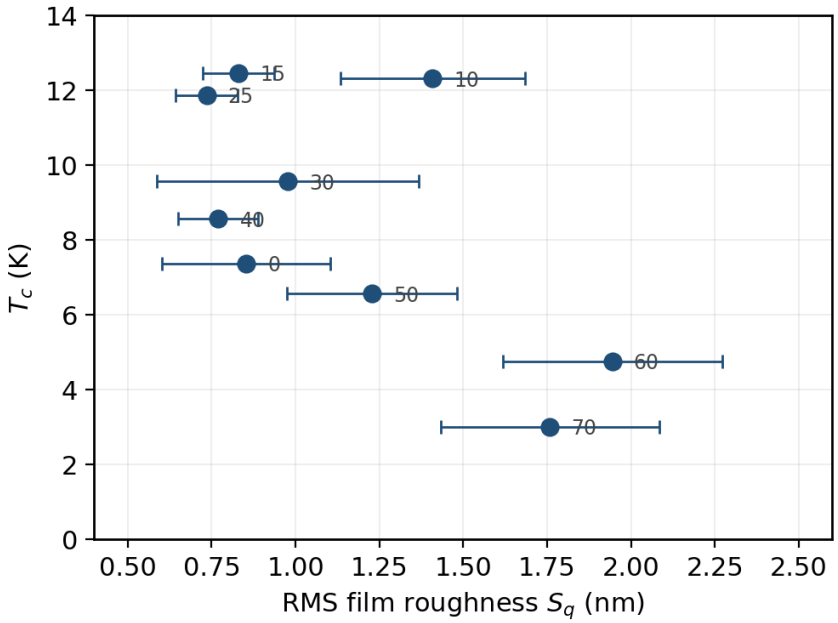


Figure 15 T_c against RMS film roughness. Labels give the N_2 pressure in mTorr. Horizontal bars are scan-to-scan standard deviations; the uncertainty belongs to the AFM quantity, not to T_c.

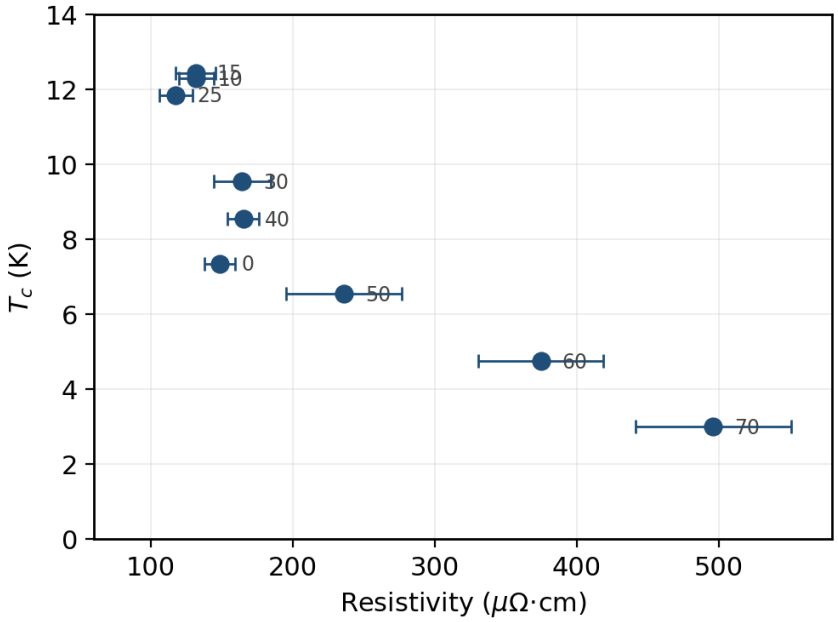


Figure 16 T_c against resistivity - the strongest correlation in the dataset, $r = -0.88$.

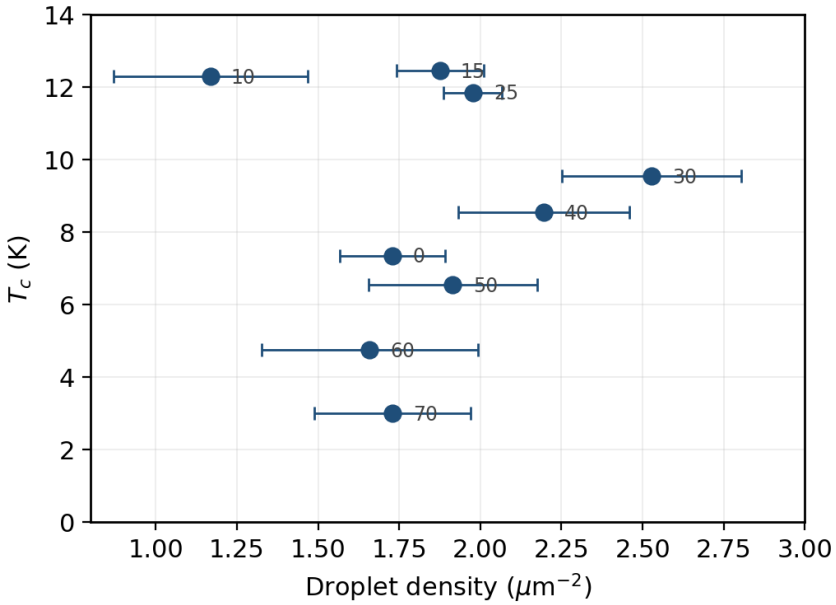


Figure 17 T_c against droplet density. No relationship is present ($r = +0.01$).

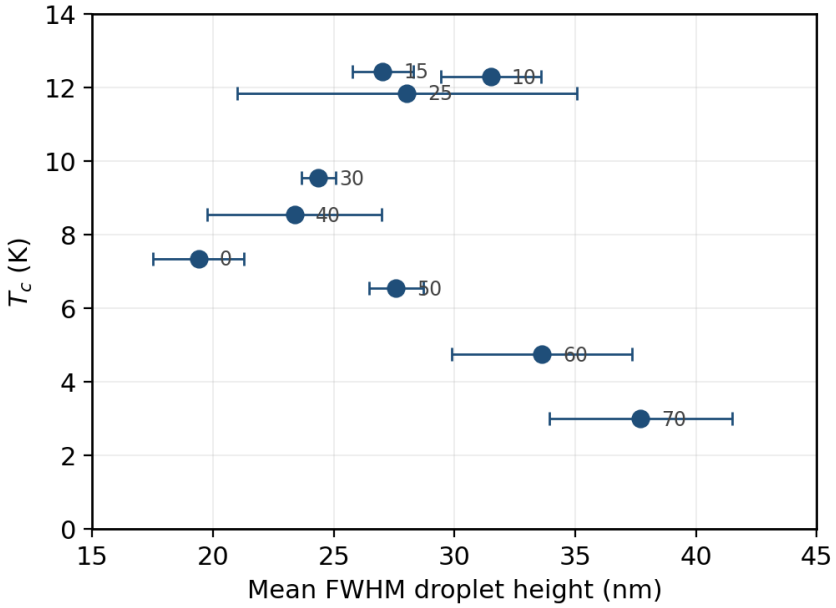


Figure 18 T_c against mean FWHM droplet height ($r = -0.39$, falling to -0.23 under the strict threshold).

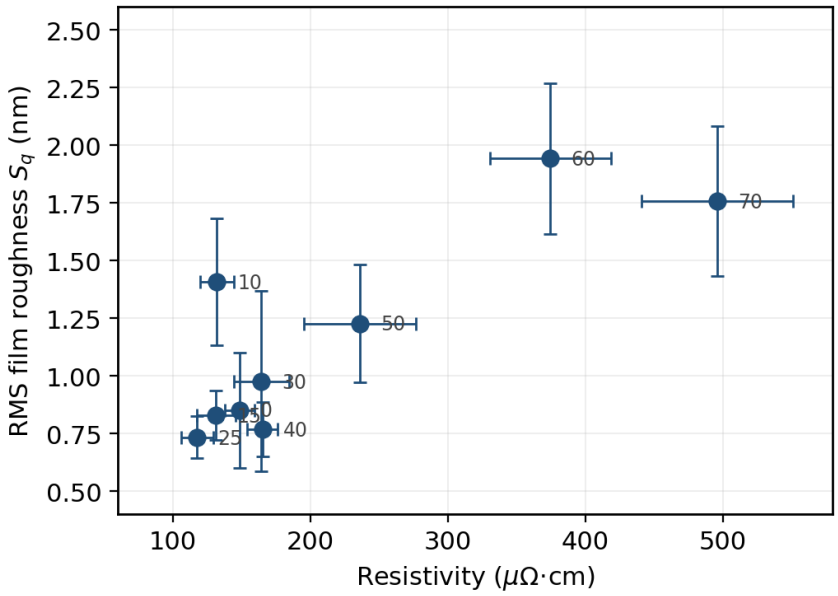


Figure 19 Film roughness against resistivity. Two independent techniques - surface topography and bulk transport - track the same underlying microstructure ($r = +0.83$).

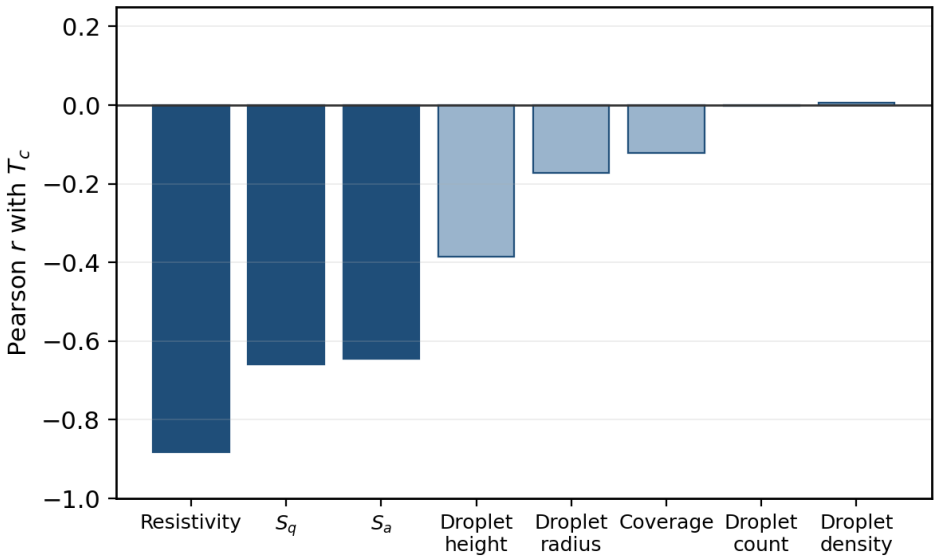


Figure 20 Pearson correlation of each measured quantity with T_c across the nine samples. The two roughness terms are separated from every droplet quantity by a clear gap.

6 Discussion

6.1 Three growth regimes, set by the plume energy

The transport, roughness and kinetic results together divide the series into three regimes, and the boundaries fall where Section 4 predicted.

Under-scattered (0-10 mTorr). The plume is essentially collisionless - fewer than seven collisions in transit at 10 mTorr - and arriving Nb still carries several eV. Adatom mobility is high and the

surface is smooth, but the flux is energetic enough to damage the film it is building. Li *et al.* describe exactly this: shot peening and sub-surface implantation, giving a dense layer under large compressive stress [2]. The 0 mTorr film, which receives the harshest flux, has both the smallest density of states at the Fermi level and the smallest lattice parameter of the five films they characterised, and reaches only 7.35 K. The limitation here is implantation damage, not composition: the film is already cubic δ-NbN.

Optimal (15-25 mTorr). The plume is slowed enough to stop damaging the film but is still energetic: 2.3 eV at 15 mTorr and 0.19 eV at 25 mTorr, both above the thermal floor. Every indicator agrees - T_c at its maximum of 12.45 K, resistivity at its minimum of 117.5 $\mu\Omega$·cm, and S_q at its minimum of 0.735 nm. That the roughness minimum and the resistivity minimum coincide, having been measured on completely different instruments, is the clearest single piece of evidence in this dataset.

Thermalised (30-70 mTorr). Above roughly 31 mTorr the arriving flux is thermalised. Adatoms now depend on substrate temperature alone for surface diffusion, which is a far weaker source of mobility than the eV they previously carried. Nucleation density rises, grains stay small, boundaries multiply and voids are no longer filled in. At the same time the reactive nitrogen fraction falls as recombination in the confined plume increases [7]. Everything degrades together: T_c falls by a factor of four, resistivity rises by 4.2, and S_q rises by 2.6.

The agreement between the estimated threshold (31^{+10}_{-7} mTorr) and the observed turning point (between 25 and 30 mTorr) should be read with care. The kinetic estimate was built from gas properties and geometry alone, without reference to the data, which makes the agreement meaningful rather than circular. But it carries a factor-of-1.5 uncertainty in either direction, and the branch correlations rest on six points above the split and three below. It is best described as a consistency check the kinetic picture passes, not a precise measurement of a threshold.

6.2 Roughness as a proxy for microstructure

It is worth being explicit about what the roughness correlation does and does not mean. The claim is not that a rough surface suppresses superconductivity directly. That said, these films are thin - 20.0 to 27.9 nm by x-ray reflectivity [2] - so an S_q of 0.7 to 2.0 nm is 3.5% to 7% of the thickness, and a geometric contribution cannot be dismissed on scale alone. What makes the geometric reading insufficient is that it would have to produce a factor-of-four change in T_c from a few percent modulation of thickness, and that it says nothing about why resistivity follows the same trend.

Roughness is better read as a *proxy*. In a columnar polycrystalline film the surface relief is the top of the grain structure: small, poorly coalesced grains with deep boundaries give a rough surface, while large, well coalesced grains give a smooth one. The quantity actually controlling T_c is the grain and defect structure underneath, and roughness is a convenient, non-destructive readout of it.

The evidence for this reading is that resistivity - a bulk transport measurement with far less sensitivity to topography - correlates with S_q at $r = +0.83$. Two independent techniques, one probing the surface and one probing electron transport through the whole film, are tracking the same thing. Treece *et al.* made the same argument from the other direction, attributing the higher resistivity of their textured films relative to epitaxial ones to grain-boundary scattering and a shorter electronic mean free path [1].

A specific mechanism for this appears in the companion paper. Treece *et al.* model the film as a granular superconductor: metallic NbN grains, each with its own T_c, separated by a thin shell of insulating nitrogen-rich Nb_3N_4 precipitated out of the grain interiors [5]. The measured resistance is then the sum of a metallic intragranular term and an insulating intergranular one, so as the shell thickens the residual resistance ratio falls and the transition broadens - both of which they observe. This maps onto the present series directly: thermalised growth above 30 mTorr produces smaller grains, hence more grain-boundary area per unit volume, hence a rougher surface, a higher resistivity and a lower T_c, all from one cause.

For completeness, and stating their conclusion rather than a paraphrase of it: Li *et al.* find that T_c tracks the out-of-plane lattice parameter almost linearly across this series, and attribute the variation to lattice strain together with the density of states $N(0)$, analysed within the Allen-Dynes strong-coupling framework [2]. They explicitly do *not* attribute it to a phase change or to stoichiometry, since the δ-NbN reflection neither shifts nor splits and the T_c modulation they see is about twice what stoichiometry alone is known to produce. Structural refinement is outside the scope of this work; what matters here is that their mechanism and the one argued above are the same mechanism seen from two sides, because the strain state they measure is set by the arrival energy this report estimates.

6.3 The null result on droplets, and why it was predictable

Droplet size, number, density and coverage show no relationship to T_c. This is a negative result and it is worth stating as a finding rather than hiding as an absence. It is supported three ways: the correlations are small ($|r| \leq 0.39$); they do not survive a change in detection threshold; and some of them change sign under that change.

Section 4.6 predicted this before the data were examined. Droplets are ballistic - their stopping distance in the background gas exceeds the target-substrate separation by more than two orders of magnitude at the highest pressure used - so nitrogen pressure has essentially no influence on their transport. They are produced by splashing at the target surface, and what governs them is target condition, laser fluence and spot quality. None of these is the variable under study.

Droplets are therefore best understood as a *deposition artefact superimposed on* the film rather than as part of it. They cover 4-9% of the surface and are visually dominant, but the superconducting properties are set by the other 91-96%, which is exactly the region on which the roughness is measured.

6.4 The droplet height drift is most likely a threshold artefact

One droplet quantity does drift with pressure: mean height, at $r = +0.67$. The histograms of Section 5.4 show this is a translation of the whole distribution rather than a change in its tail - at 70 mTorr the population of droplets shallower than 10 nm present at 0 mTorr has gone - so it is a real feature of the measurement rather than an artefact of averaging. The question is what produces it.

The obvious explanation is a target-side one. Prolonged exposure to nitrogen nitrides the target surface, and a nitrided surface has different optical and thermal properties, which would change how it splashes.

A second explanation fits better, and it is instrumental rather than physical. The detection thresholds are multiples of the film's own texture, so on a rougher film the effective minimum

detectable droplet height rises and shallow droplets are rejected. If that is what is happening, median droplet height should track S_q rather than pressure. It does:

- median droplet height against S_q: $r = +0.893$
- median droplet height against pressure: $r = +0.655$
- the ratio (median height)/S_q is 19.8 ± 4.3, constant to about 20% across the series

The decisive point is the 10 mTorr sample. It breaks the monotonic pressure trend in roughness, being anomalously rough at $S_q = 1.408$ nm, and the droplet height rises with it to a median of 25.5 nm - higher than at 30 or 40 mTorr, where the pressure is greater but the film is smoother. Pressure alone cannot produce that ordering; S_q can.

If this reading is right, the one apparent exception to the null result is not an exception at all: it is the detector responding to the film beneath the droplets rather than to the droplets themselves. That strengthens the main argument. The two explanations are not mutually exclusive, and with nine samples a common-cause account cannot be excluded; the claim made here is only that the threshold explanation accounts for more of the structure in the data. The test is simple: re-run the detector with an absolute height threshold in nanometres instead of a texture-relative one. If the drift disappears, it was the threshold.

Either way, droplet height still shows no useful relationship to T_c ($r = -0.39$, falling to -0.23 under the strict threshold).

7 Conclusion

Across nine NbN films grown on MgO by pulsed laser deposition at 0-70 mTorr N_2, the RMS roughness of the film surface measured *between* the deposition droplets is the only morphological parameter that tracks the superconducting transition temperature. It correlates with T_c at $r = -0.66$ and with resistivity at $r = +0.83$, and it is the only surface parameter whose correlation survives - and slightly strengthens under - a change in the droplet detection threshold. Droplet size, number, density and coverage all give $|r| \leq 0.39$, and these values weaken or change sign when the threshold is changed. This is presented as a well-supported null result rather than as a weak correlation.

Gas kinetics predicts the contrast in advance. Starting from the ≤ 100 eV plume energies reported for PLD of this material, an ablated NbN unit loses about a third of its energy per collision with N_2 and needs roughly twenty collisions to thermalise, which over a 50 mm throw corresponds to a threshold pressure of 31^{+10}_{-7} mTorr. Droplets, by contrast, have a stopping distance of several metres in the same gas and are ballistic throughout. The gas therefore controls the flux that builds the film but not the flux that produces the droplets, and only the first of these correlates with T_c.

Consistent with this, T_c peaks at 12.45 K at 15 mTorr while resistivity and roughness both reach their minima at 25 mTorr, and above 25-30 mTorr all three degrade together. Structural data on the same films support the reading: at fixed pulse count the films grow thicker with pressure, and thickness tracks resistivity and roughness together, which is the signature of a change to porous columnar growth rather than of any change in the droplets.

The measurable that matters on a PLD nitride surface is therefore the roughness of the film *between* the droplets, not the droplets themselves. The physical reason is that the background gas thermalises the atomic flux that builds the film while leaving the ballistic droplet flux untouched. Whole-image roughness, which mixes the two, discards the signal.

A Full Set of Droplet Size Distributions

All distributions are pooled over every scan of the sample, all-droplets analysis. Every figure uses identical axes and is normalised to the percentage of that sample's droplets per bin, so panels may be compared directly; the dotted line marks the median. Note that the lowest radius bins are shaped by the 37.4 nm pixel size rather than by the droplets, which is the reason the strict analysis of Section 3 exists.

A.1 Radius distributions

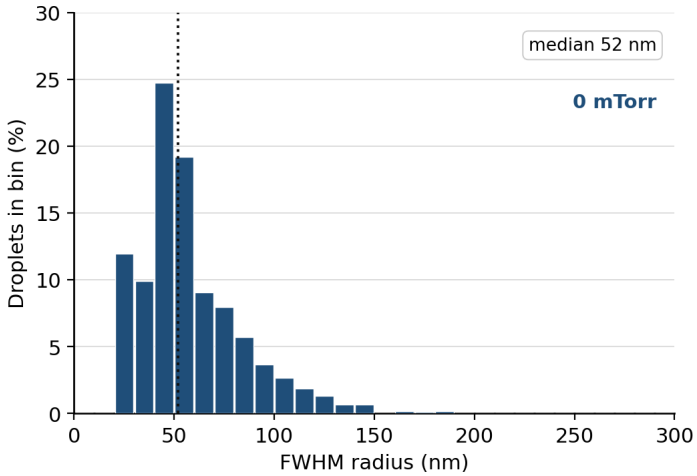


Figure 21 Droplet radius distribution at 0 mTorr (median 52 nm).

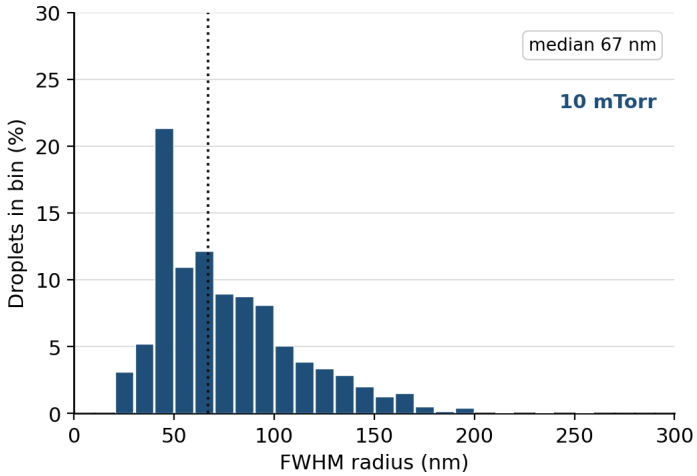


Figure 22 Droplet radius distribution at 10 mTorr (median 67 nm).

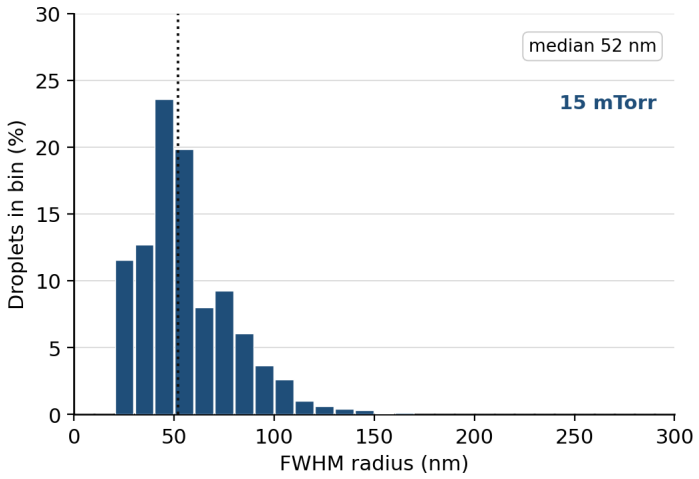


Figure 23 Droplet radius distribution at 15 mTorr (median 52 nm).

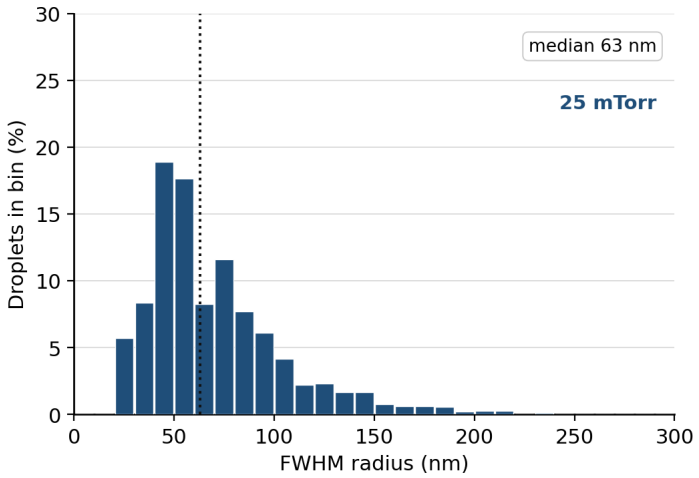


Figure 24 Droplet radius distribution at 25 mTorr (median 63 nm).

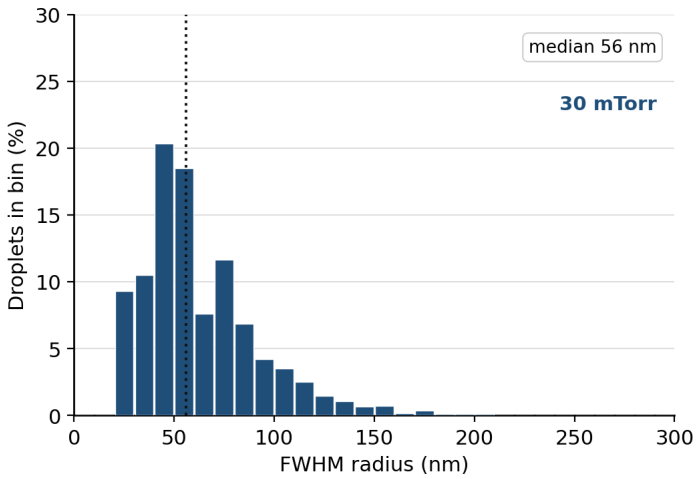


Figure 25 Droplet radius distribution at 30 mTorr (median 56 nm).

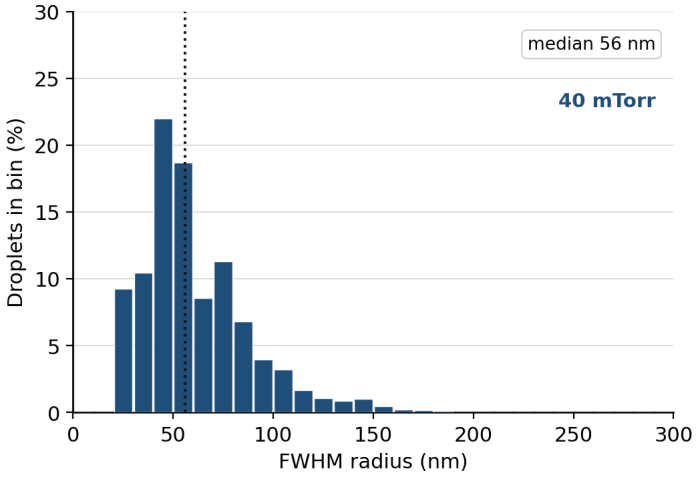


Figure 26 Droplet radius distribution at 40 mTorr (median 56 nm).

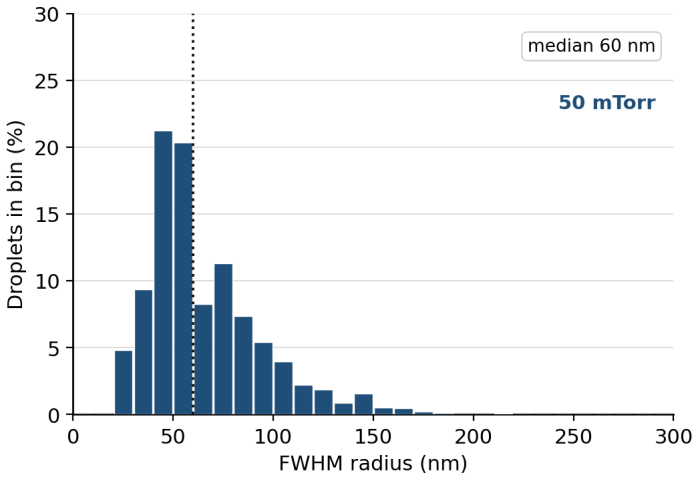


Figure 27 Droplet radius distribution at 50 mTorr (median 60 nm).

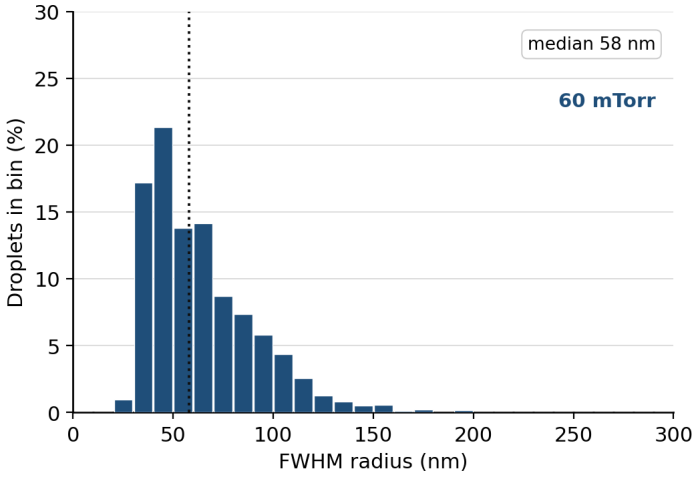


Figure 28 Droplet radius distribution at 60 mTorr (median 58 nm).

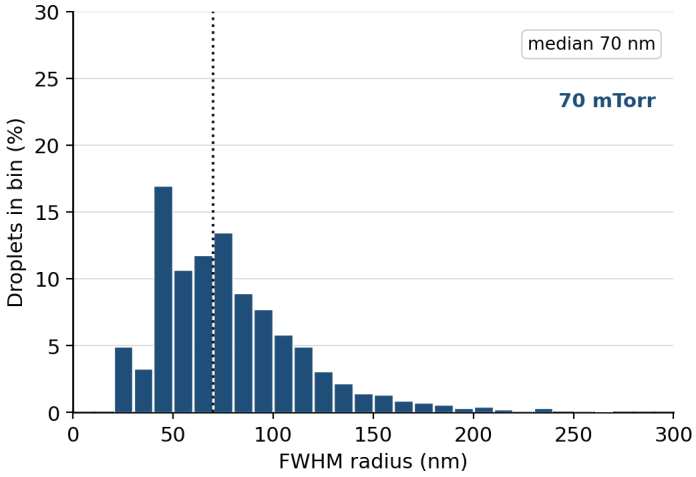


Figure 29 Droplet radius distribution at 70 mTorr (median 70 nm).

A.2 Height distributions

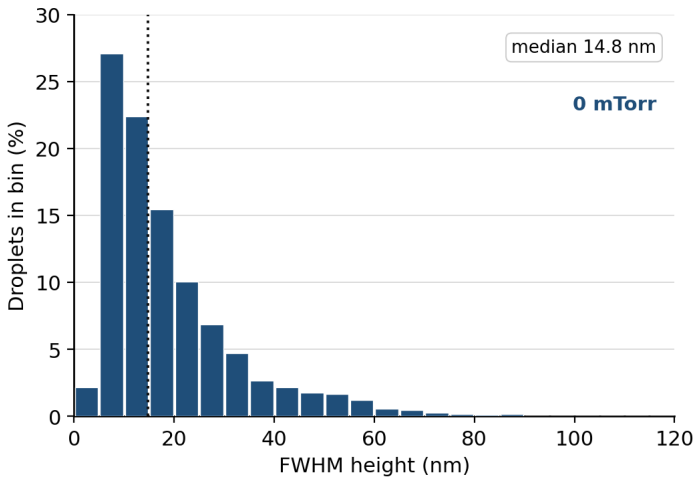


Figure 30 Droplet height distribution at 0 mTorr (median 14.8 nm).

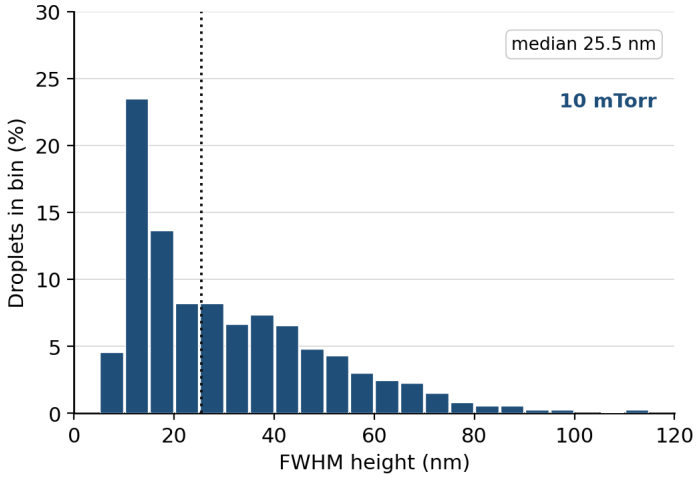


Figure 31 Droplet height distribution at 10 mTorr (median 25.5 nm).

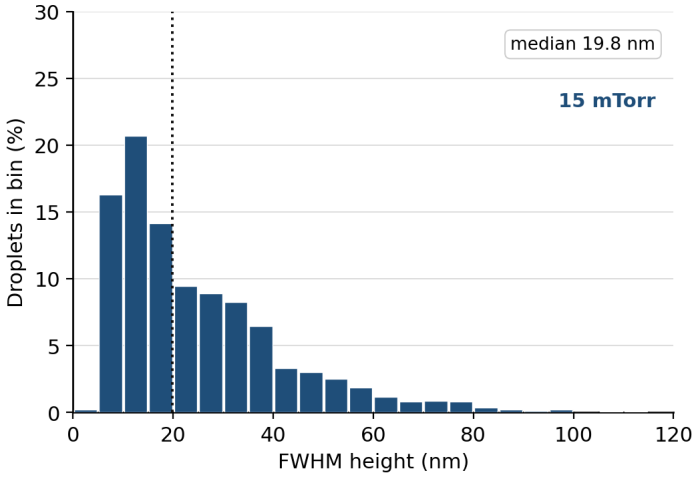


Figure 32 Droplet height distribution at 15 mTorr (median 19.8 nm).

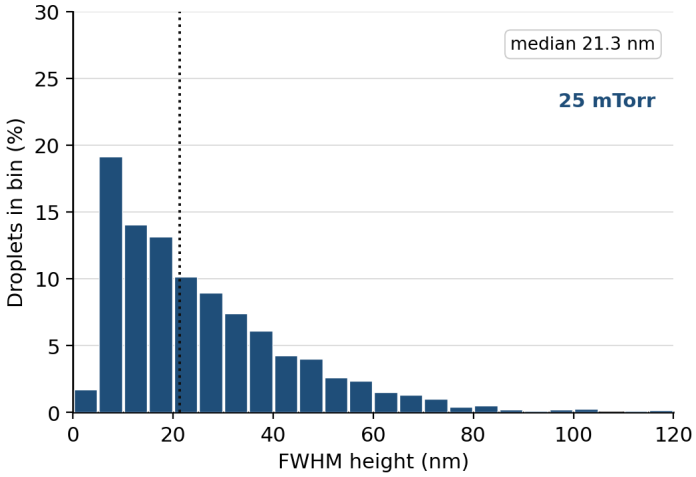


Figure 33 Droplet height distribution at 25 mTorr (median 21.3 nm).

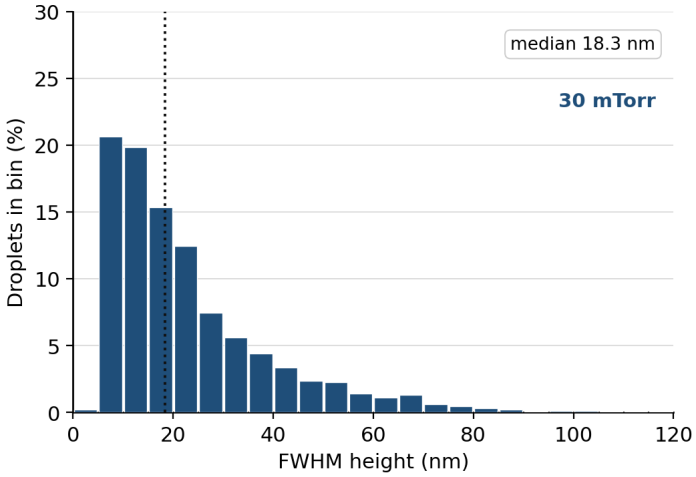


Figure 34 Droplet height distribution at 30 mTorr (median 18.3 nm).

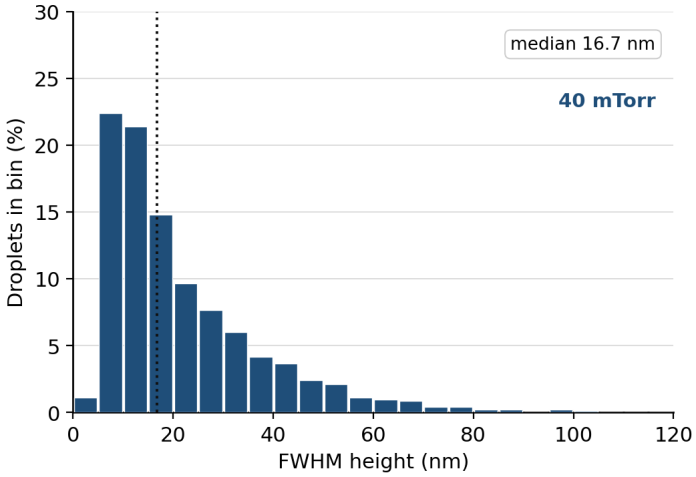


Figure 35 Droplet height distribution at 40 mTorr (median 16.7 nm).

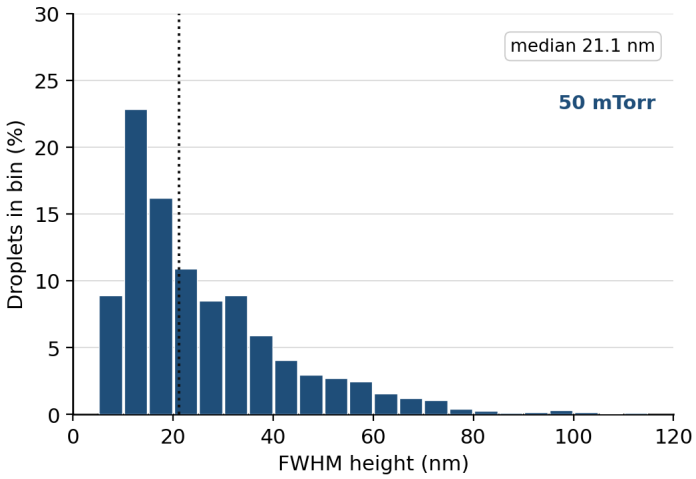


Figure 36 Droplet height distribution at 50 mTorr (median 21.1 nm).

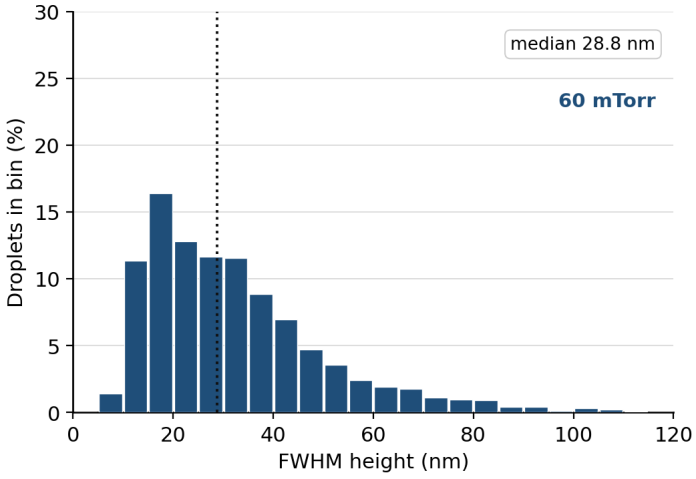


Figure 37 Droplet height distribution at 60 mTorr (median 28.8 nm).

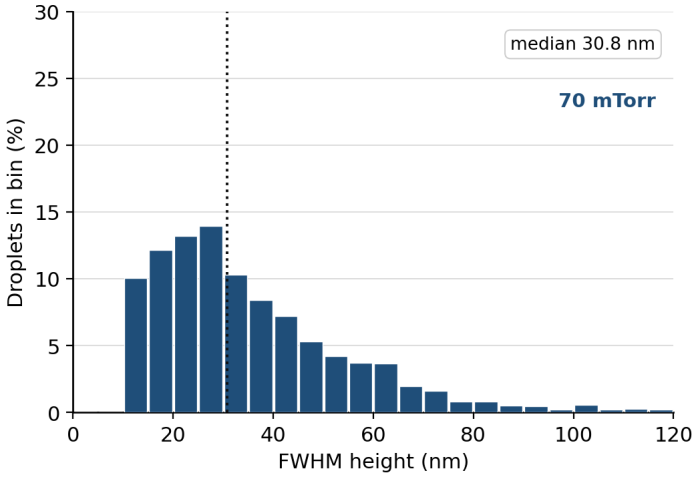


Figure 38 Droplet height distribution at 70 mTorr (median 30.8 nm).

References

[1] Randolph E. Treece et al. "Pulsed laser deposition of high-quality NbN thin films". In: *Applied Physics Letters* 65.22 (1994), pp. 2860–2862. DOI: 10.1063/1.112516.

[2] Zeyou Li et al. "Transport and structural characterisation of pulsed-laser-deposited NbN thin films". In: *Superconductor Science and Technology* 39.5 (2026), p. 055007.

[3] Louis E. Toth. *Transition Metal Carbides and Nitrides*. New York: Academic Press, 1971.

[4] Douglas B. Chrisey and Graham K. Hubler, eds. *Pulsed Laser Deposition of Thin Films*. New York: John Wiley & Sons, 1994.

[5] Randolph E. Treece et al. "New phase of superconducting NbN stabilized by heteroepitaxial film growth". In: *Physical Review B* 51.14 (1995), pp. 9356–9359. DOI: 10.1103/PhysRevB.51.9356.

[6] P. R. Willmott and J. R. Huber. "Pulsed laser vaporization and deposition". In: *Reviews of Modern Physics* 72.1 (2000), pp. 315–328.

[7] Ashraf Hassan Farha et al. "Pulsed Laser Deposition of Niobium Nitride Thin Films". In: *AIP Conference Proceedings*. Vol. 1687. 2015, p. 020003. DOI: 10.1063/1.4935317.